The Periplasmic Domain of TolR from *Haemophilus influenzae* Forms a Dimer with a Large Hydrophobic Groove: NMR Solution Structure and Comparison to SAXS Data[†,‡]

Lisa M. Parsons, Alexander Grishaev, and Ad Bax*

Laboratory of Chemical Physics, National Institute of Diabetes and Digestive and Kidney Diseases, National Institutes of Health, 5 Memorial Drive, Bethesda, Maryland 20892

Received November 15, 2007; Revised Manuscript Received January 7, 2008

ABSTRACT: TolR is a part of the Pal/Tol system which forms a five-member, membrane-spanning, multiprotein complex that is conserved in Gram-negative bacteria. The Pal/Tol system helps to maintain the integrity of the outer membrane and has been proposed to be involved in several other cellular processes including cell division. Obtaining the structure of TolR is of interest not only to help explain the many proposed functions of the Pal/Tol system but also to gain an understanding of the TolR homologues ExbD and MotB and to provide more targets for antibacterial treatments. In addition, the structure may provide insights into how colicins and bacteriophages are able to enter the cell. Here we report the solution structure of the homodimeric periplasmic domain of TolR from *Haemophilus influenzae*, determined with conventional, NOE-based NMR spectroscopy, supplemented by extensive residual dipolar coupling measurements. A novel method for assembling the dimer from small-angle X-ray scattering data confirms the NMR-derived structure. To facilitate NMR spectral analysis, a TolR construct containing residues 59–130 of the 139-residue protein was created. The periplasmic domain of TolR forms a C_2-symmetric dimer consisting of a strongly curved eight-stranded β-sheet, generating a large deep groove on one side, while four helices cover the other face of the sheet. The structure of the TolR dimer together with data from the literature suggests how the periplasmic domain of TolR is most likely oriented relative to the cytoplasmic membrane and how it may interact with other components of the Pal/Tol system, particularly TolQ.

The Pal/Tol proteins found in Gram-negative bacteria are highly conserved and are thought to be involved in several key cellular processes, but as of yet the specifics of how they function are unknown. They are expressed from an operon which generally encodes at least five proteins, TolA, TolQ, TolR, TolB, and Pal; however, the gene encoding TolA does not appear to be as conserved as the others (*1*). The five conserved Tol/Pal proteins interact to form a link between the inner and outer membranes (Figure 1). Starting at the inner membrane, the membrane-spanning proteins TolQ, TolR, and the N-terminus of TolA form a complex (*2*). TolA has a long predicted helical second domain that is thought to stretch across the periplasm where its C-terminal domain interacts with the N-terminal domain of TolB (*3, 4*). The C-terminal domain of TolB forms a six-bladed β-propeller and competes with peptidoglycan to bind Pal, which is associated with the outer membrane via a lipid modification of its N-terminal cysteine. In addition, Pal can be cross-linked to TolA in the presence of a proton motive force (PMF) (*5*). Knocking out any of these proteins affects the integrity of the outer membrane, resulting in enhanced sensitivity to

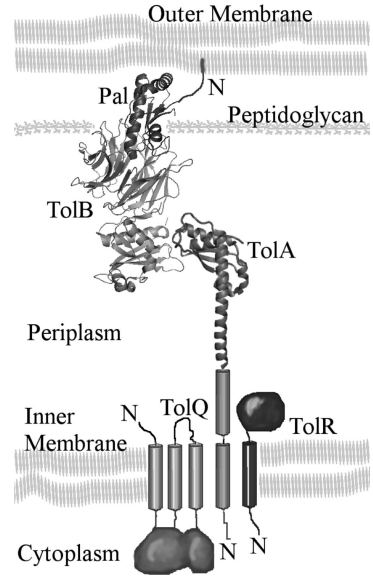

FIGURE 1: Schematic model of the Pal/Tol system of proteins, incorporating the X-ray structures for the *E. coli* Pal/TolB complex (PDB code 2HQS) and the C-terminal domain of TolA from *P. aeruginosa* (PDB code 1LR0). Proposed transmembrane helices and helical domains (TolA) are shown as tubes.

[†] This work was supported by the Intramural Research Program of the NIDDK, NIH, and by the Intramural AIDS-Targeted Antiviral Program of the Office of the Director, NIH. L.M.P. was supported by a PRAT fellowship from NIGMS.

[‡] NMR structures of TolR without SAXS data are deposited under PDB code 2JWK. The structures calculated with NMR and SAXS data are under PDB code 2JWL. Chemical shift assignments can be found in the BMRB under code 15459.

* Corresponding author. Phone: 301-496-2848. Fax: 301-402-0907. E-mail: bax@nih.gov.

10.1021/bi702283x CCC: $40.75
Published on Web 02/12/2008

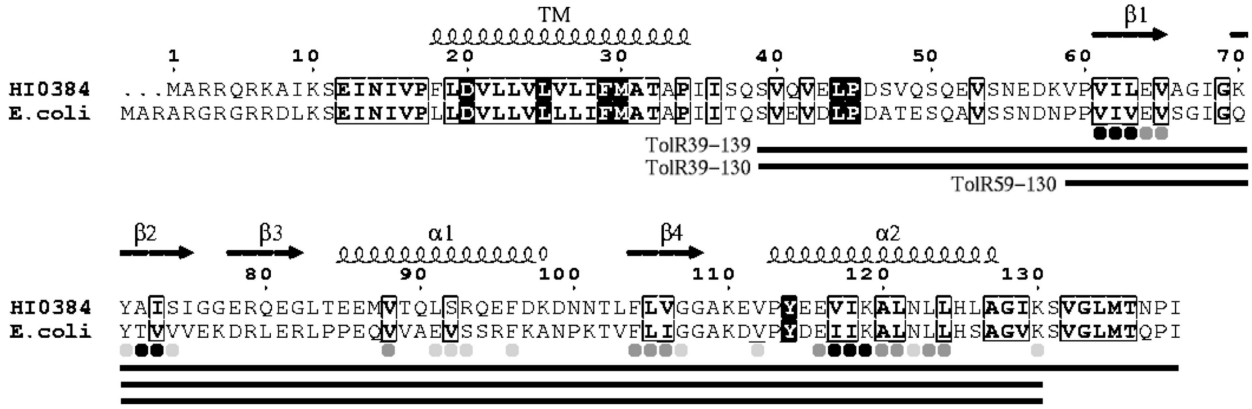

FIGURE 2: Amino acid conservation of 106 homologues of TolR. Sequences for *H. influenzae* (HI0384) and *E. coli* are shown. The secondary structure for HI0384 is above the sequences. TM = predicted transmembrane helix. White letters in black are 100% conserved. Black letters in clear boxes have equivalent residues in 90% or greater of the sequences. Dots below the sequences depict deuterium exchange data for TolR59–130: black dots, amide protons present longer than 3 h; medium gray dots, present greater than 1 h; light gray dots, present longer than 15 min. Solid black lines below the sequences mark residues in HI0384 used in different TolR clones.

detergents, the release of periplasmic proteins, and blebbing of the outer membrane (*6–8*).

In addition to maintaining membrane integrity, the Pal/Tol proteins and their homologues participate in several other processes. A recent, very intriguing finding was that the Pal/Tol proteins in *Escherichia coli* appear to be involved in cell division as their presence is required for the proper invagination of the outer membrane (*9*). TolQ and TolR are homologous to the ExbB and ExbD proteins which, in conjunction with TonB, activate iron siderophore and vitamin B_{12} transporters in the outer membrane via the PMF[1] of the cytoplasmic membrane. TonB is not noticeably homologous to TolA, yet the TolQ/TolR and ExbB/ExbD pairs can cross-complement one another (*10*). In addition, in *E. coli*, both protein complexes are utilized by colicins (bacterially produced toxins) to gain access to the cell: group A colicins enter via the Pal/Tol proteins and group B via the Ton/Exb system (*2, 11*). The proposed role for the ExbB/ExbD complex is to bring TonB back to the cytoplasmic membrane after energy transduction at the outer membrane is complete (*12*). It has also been suggested, based on weak sequence homology to the MotA and MotB proteins of the flagellar motor and mutational analysis of TolQ and TolR, that the TolQ/TolR inner membrane complex forms an ion channel (*13, 14*). Additionally, the study of homologues in *Pseudomonas putida* indicates that knocking out any of the Pal/Tol proteins affects the uptake of various carbon sources (*15*).

In addition to their interesting functional properties, proteins in the Pal/Tol and Exb/TonB complexes may play a role in the current fight against antibiotic-resistant bacteria. Pal is a vaccine candidate for nontypeable *Haemophilus influenzae* in part because humans make bactericidal antibodies after exposure to the bacteria (*16*). TolA, TolR, and TolQ are required for entrance of f1 bacteriophage while TonB, ExbB, and ExbD are involved in the entrance of phage H8 (*17–19*). Since bacteriophages and phage proteins can be used to treat bacterial infections even in antibiotic-resistant bacteria (*20*), knowledge of their mechanism of entrance may prove to be very important.

[1] Abbreviations: RDC, residual dipolar coupling; SAXS, small-angle X-ray scattering; NOE, nuclear Overhauser enhancement; PMF, proton motive force; rmsd, root mean square difference.

In recent years the structures of Pal, TolB, and the C-terminus of TolA have been solved, providing insight into protein–protein and protein–ligand interactions, but there is still little structural information on the TolA/TolR/TolQ inner membrane complex (*21–23*). It is known that TolQ has three transmembrane helices and two large cytoplasmic loops or domains totaling about 150 amino acids (*24*). TolR has one transmembrane domain and a periplasmic portion thought to contain two domains, one of which interacts with or inserts into the inner membrane (*25*). The total composition of the complex is unknown, but current estimates suggest it is composed of one transmembrane helix from TolA, two TolR molecules, and four TolQ molecules (*26*).

After completing the solution structure of Pal bound to peptidoglycan (*21*), we decided to further explore proteins in this functionally interesting group by studying the solution structure of the periplasmic domain of TolR, the aim being to provide a starting point both for understanding the function of the inner membrane complexes of the Tol proteins and their homologues and to contribute to the structure elucidation of the entire complex. Here we present the structure of TolR and propose a model to explain how the periplasmic domain of TolR interacts with the membrane and with TolQ based on mutational data reported in the literature. Our solution NMR study is carried out using conventional, NOE-based multidimensional isotope-edited and isotope-filtered NMR spectroscopy, supplemented by a large number of backbone residual dipolar couplings (RDCs), and also evaluates the impact of small-angle X-ray scattering data on the accuracy of the structure.

EXPERIMENTAL PROCEDURES

Cloning. The gene for TolR from *H. influenzae* KW20 was amplified from genomic DNA using PCR and inserted into the vector pET28a (Novagen) with a $(His)_6$ tag followed by the native *E. coli* GST gene, a thrombin cleavage site, and the TolR gene, HI0384. The GST portion of the construct was included to enhance expression levels. Several clones were constructed, all without the N-terminal transmembrane helix. TolR39–139 started at Ser39 and ended at the native C-terminus. TolR39–130 started at Ser39 and ended at Lys130. TolR59–130 started at Val59 and ended at Lys130 (Figure 2).

Expression and Purification. Protein was expressed by IPTG induction using *E. coli* BL21star(DE3) cells grown at 37 °C to an OD_{600} of ~1.0 in ^{15}N- or $^{15}N/^{13}C$-labeled M9 medium. Triply labeled ($^{2}H/^{15}N/^{13}C$) TolR39–139 was produced by performing the expression in media made with 100% D_2O but using protonated [$^{13}C_6$]glucose.

Cells were harvested by centrifugation for 5 min at 10000*g* and lysed by sonication. After the lysate was centrifuged for 25 min at 25000*g* to remove insoluble material, the protein was purified using a Qiagen Ni^{2+} affinity column per the manufacturer's instructions. The affinity tag was removed by thrombin cleavage after eluting the protein from the column and dialyzing it into 25 mM Tris and 50 mM NaCl (pH 7.6) or by on-column cleavage whereby the thrombin was added directly to the column after a wash with 25 mM sodium phosphate and 150 mM NaCl (pH 8.0). When following this latter procedure, to ensure the thrombin was evenly distributed throughout the column, the outflow tube was attached to the top of the column and the buffer recirculated slowly overnight at 25 °C. The advantage of this method was that it saved time by avoiding several dialysis steps and reequilibration and loading of the column; in the morning the cleaved protein in the buffer was separated from the bound $(His)_6$-GST tag by washing the column with 50 mM sodium phosphate, 300 mM NaCl, and 20 mM imidazole, pH 8.0. The wash fraction containing TolR was then run over a consecutively attached benzamidine−agarose column to remove the thrombin. The disadvantage was that cleavage was not always complete, especially in the TolR59–130 clone which had very few amino acids between the tag and the structured domain. Instead, for TolR59–130 thrombin cleavage was performed on eluted, dialyzed samples at room temperature overnight. The protein was then dialyzed back into 50 mM sodium phosphate, 300 mM NaCl, and 10 mM imidazole, pH 8.0, and passed for a second time over the Ni^{2+} column to remove the GST tag and a consecutively connected benzamidine column to remove the thrombin. The protein was concentrated to at least 0.5 mM and dialyzed into NMR buffer: 50 mM sodium phosphate, 50–100 mM NaCl, and 0.5 mM EDTA (pH 6.7). To collect intersubunit NOE restraints, a mixed sample was made by combining equimolar amounts of $^{13}C/^{15}N$-labeled protein and unlabeled protein. On the basis of the presence of intersubunit cross-peaks in the filtered experiment, an overnight equilibration was sufficient to ensure proper mixing of the sample. Samples in D_2O were made by lyophilizing prepared NMR samples and then dissolving the dried samples in D_2O. RDC measurements were carried out on samples containing 10.0 mg/mL filamentous phage Pf1 (*27*).

NMR Experiments. All experiments were conducted at 303 K on Bruker 600 MHz spectrometers equipped with cryogenic triple-resonance probe heads containing a *z*-axis pulsed field gradient accessory. Unless referenced separately, the experiments used are described by Cavanagh et al. (*28*). The following experiments were used to make chemical shift assignments for the protein backbone and side-chain atoms: ^{15}N-HSQC, ^{13}C-HSQC, HNCACB, CBCACONH, HCCO-NH, CCONH, HCCH-TOCSY, and HNCO. For intrasubunit NOE assignments, ^{15}N-edited NOESY-HSQC and ^{13}C-edited NOESY-HSQC spectra in water and D_2O were used. Intersubunit NOE restraints were obtained from a ^{13}C-separated NOESY-HSQC in D_2O carried out on a mixed sample, with a ^{13}C filter applied at the beginning of the experiment, and from the original ^{15}N-edited NOESY-HSQC after the dimer interface was identified. For all NOE experiments a mixing time, T_m, of 150 ms was used. RDC data for the $N-H_N$ and $C'-C^\alpha$ vectors were collected from 3D HNCO experiments either without $^1H^N$ decoupling in the ^{15}N dimension or without a $^{13}C^\alpha$ decoupling pulse in the $^{13}C'$ dimension. The RDC data for $C^\alpha-H^\alpha$ vectors were collected from a H^α-coupled 3D HNCOCA experiment. The $N-C'$ RDC data were obtained from a 3D HNCO quantitative-*J* experiment (*29*). Lower limits for the experimental uncertainties for the $^{15}N-^1H$, $^{13}C'-^{13}C^\alpha$, and $^{13}C^\alpha-^1H^\alpha$ RDCs were estimated to be 0.88, 0.26, and 6.2 Hz, respectively, on the basis of the average signal-to-noise ratios and line widths (*30*). The error in the $^{15}N-^{13}C'$ RDCs was estimated to be 0.1 Hz, based on an average signal-to-noise ratio of 68:1 in the reference spectrum (*29*).

The χ_1 angles for the aromatic residues were determined from $C'-\{C^\gamma\}$ and $N-\{C^\gamma\}$ spin–echo difference ^{15}N HSQC experiments (*31*). ^{15}N T_1, T_2, and NOE relaxation data were acquired with relaxation delays of 20, 196, 404, 580, 804, and 996 ms for T_1; 8, 16, 40, 60, 120, and 160 ms for T_2; and an overall delay of 6 s prior to the first ^{15}N pulse of the NOE experiment (*32*). Deuterium exchange was followed by recording ^{15}N HSQC spectra on a lyophilized sample rehydrated in 99.9% D_2O.

Force Constant Determination and Cross-Validation for RDCs. Considering that the error for each of the four RDC types was less than 12% of the total range available to each coupling, the RDC measurement error for none of the four types of couplings limits the accuracy of the structure until free *Q*-factors drop well below 30%, a level not commonly achieved in the absence of extensive RDC measurements (*33, 34*). Therefore, in a first iteration, all force constants for the normalized RDCs (relative to $^1D_{NH}$) were set to the same value, and a range of force constants was explored, increased stepwise from 0.125 to 8.0 kcal mol^{-1} Hz^{-2} in multiples of 2. At each force constant setting five structures were calculated, each using a different set of 80% of the $N-H^N$ RDCs as well as the full complement of the other RDCs. *Q*-factors for the remaining 20% of the $N-H^N$ RDCs not used in the structure were then calculated, averaged, and plotted to find the force constant for $N-H^N$ that gave the lowest *Q*-factor. A force constant of 0.6 kcal mol^{-1} Hz^{-2} gave optimal results and is close to the value found by Garrett and Clore (*35*). Optimization of the force constants for the other RDCs was probed by doubling and halving their force constant in separate sets of structure calculations, again using 20% sets of randomly selected $^1D_{NH}$ RDCs to evaluate structural accuracy.

Data Processing and Structure Calculations. Data were processed using NMRPipe (*36*) and examined using Sparky (*37*) software packages. Some NOE assignments were automatically selected using NOEID (*38*). Backbone dihedral angle restraints were obtained using TALOS (*29*) and used with error values set to the larger of three times the standard deviation or ±20°. Side-chain χ_1 restraints for the five aromatic residues were obtained from $^3J_{C'-C\gamma}$ and $^3J_{N-C\gamma}$ measurements, with each residue clearly occupying a single well-defined rotameric state. Figures depicting the structure were made by PyMOL (*39*).

Structures were calculated initially from an extended polypeptide chain using CNS 1.1 utilizing standard simulated annealing and torsion angle dynamics and later from the resulting folded structures (*40*). Hydrogen bonds were initially entered on the basis of deuterium exchange and secondary structure information but were later removed and determined using the hydrogen-bonding potential (HBDB) function in CNS with a directional force of 0.75 and a linearity force of 0.25 (*41*). Hydrogen bonds consistently selected in the "free" mode by HBDB were subsequently used as fixed restraints. The latter prevents hydrogen bonds from occasionally not being selected by HBDB. Distance restraints based on NOE peak intensities were categorized as strong (1.8−3.2 Å), medium strong (1.8−3.8 Å), medium (1.8−4.2 Å), medium weak (2.0−5.0 Å), weak (2.5−5.5 Å), and very weak (3.0−6.0 Å). An average of 17 interresidue NOEs per residue was assigned. Structural analysis was performed using Procheck (*42*), MolProbity (*43*), and DC, a program for analyzing RDC restraints which is part of the NMRPipe software package (*36*). Final force constants were 1000 kcal mol^{-1} Å^{-2} for bond lengths, 500 kcal mol^{-1} rad^{-2} for angles and improper torsions, 40 kcal mol^{-1} Å^{-2} for experimental distance restraints, 200 kcal mol^{-1} rad^{-2} for dihedral angle restraints, and 4.0 kcal mol^{-1} Å^{-4} for the van der Waals repulsion term. Force constants for RDC restraints (not normalized to $^1D_{NH}$) were 0.6 kcal mol^{-1} Hz^{-2} for N−H^N, 0.15 kcal mol^{-1} Hz^{-2} for C$^\alpha$−H$^\alpha$, 15 kcal mol^{-1} Hz^{-2} for C$^\alpha$−C′, and 20 kcal mol^{-1} Hz^{-2} for N−C′. The 20 best structures were chosen on the basis of a low total energy, no NOE distance violations greater than 0.5 Å, no dihedral restraint violations greater than 5 deg, fewer than 10 bad contacts per 100 residues (as calculated by Procheck), and a dihedral *G*-factor greater than −0.5 (as calculated by Procheck). A list of the types of restraints used as well as the structural statistics can be found in Table 1. A backbone overlay of the 20 best structures and charts depicting the rmsd and number of NOEs per residue are presented in Figure 3.

Table 1: NMR and Refinement Statistics

	no SAXS	with SAXS
NMR Distance and Dihedral Constraints per Monomer		
distance restraints		
total NOE	2441	
intraresidue	1221	
interresidue		
sequential ($\|i-j\|=1$)	490	
medium range ($\|i-j\|\leq 4$)	344	
long range ($\|i-j\|>4$)	321	
intersubunit	65	
HBDB[a]	44	
dihedral restraints	121	
RDC restraints	263	
Structure Statistics		
rmsd from exptl restraints (mean and SD)		
Q-factor (%)	20.0 ± 0.2	19.1 ± 0.2
distances (Å)	0.015 ± 0.0005	0.015 ± 0.0005
torsion angles (deg)	0.061 ± 0.044	0.009 ± 0.007
deviations from idealized geometry		
bond lengths (Å)	0.0038 ± 0.0001	0.004 ± 1.0e^{-6}
bond angles (deg)	0.68 ± 0.01	0.69 ± 0.004
impropers (deg)	0.56 ± 0.01	0.59 ± 0.007
HBDB energies (kT)		
$E(r,\theta,\varphi)$	−4.58 ± 0.05	−4.67 ± 0.03
$E(\theta''\|r)$	0.43 ± 0.04	0.46 ± 0.02
Procheck Ramachandran distribution		
core	96.5 ± 1.1	94.2 ± 1.0
allowed	3.5 ± 1.1	5.8 ± 1.0
generous and disallowed	0.0	0.0
other Procheck statistics		
bad contacts per monomer	0.0	1.9 ± 0.9
G-factor	0.21 ± 0.02	0.16 ± 0.01
MolProbity clash score	7.83 ± 1.57	9.14 ± 1.41
average pairwise rmsd (Å)[b]		
all	0.66 ± 0.28	0.42 ± 0.16
backbone (N, C$^\alpha$, C′)	0.27 ± 0.24	0.17 ± 0.09

[a] Fixed hydrogen bond restraints consistently found by HBDB. [b] Pairwise rmsd was calculated among 20 refined structures.

SAXS Data Collection. Small angle X-ray scattering data were collected on a SAXSess instrument from Anton Paar, designed as a Kratky camera equipped with high-flux multilayer optics. X-ray radiation from a sealed fine-focus tube source (Princeton Instruments), operating at 40 kV and 50 mA, was monochromated at the Cu Kα wavelength (1.542 Å) and incident on the sample in a 1 mm inner diameter quartz capillary of 10 mm length, thermostated at 25 °C. A line-shaped X-ray beam 9 mm in length was used to maximize the incident flux. Sample conditions were the same as used for NMR data acquisition, except 150 mM of NaCl was used in order to suppress the effects of interparticle correlations (structure factor). Data were collected as series of sequential 2 h acquisitions with the protein sample first, followed immediately by the dialysis buffer. Due to signal relaxation, the imaging plates were read out with a 5 min delay at the end of each acquisition session. Since the imaging plate is mounted on a cylindrical railing during data acquisition, no corrections for detector skew were necessary. Data at two protein concentrations (8 and 4 mg/mL) were collected in order to investigate the magnitude of the interparticle structure factor. Wide-angle scattering data were collected within the *q*-range from ∼0.02 to ∼2.80 Å^{-1}. Here, $q = 4\pi \sin(\theta)/\lambda$, where 2θ is the scattering angle and λ is the wavelength of the incident radiation. The recorded 2D images were converted to 1D scattering profiles by radial integration within 5 mm strips aligned at the center of the incident beam. The 1D profiles were then mapped onto the *q*-axis by reference to the position of the primary beam attenuated by the semitransparent beam stop of the instrument. The converted profiles were corrected for the readout noise of the imaging plate scanner and normalized to the recorded intensities of the transmitted primary beam. The scattering curves from the buffer were then subtracted from the scattering curve of the protein sample. The final scattering data were averaged over three independent sample/buffer data acquisitions of 2 h each. The line-collimation 1D profiles were desmeared using GNOM software (*44*), taking into account the recorded length profile of the incident beam. The resulting point collimation-like data were used for the subsequent structural analysis in the *q* interval from 0.02 to 0.60 Å^{-1} (crystallographic resolutions between ∼300 and ∼10 Å). Evaluations of the quality of the fit of the scattering data to the various structural models were made with Crysol version 2.5 (*45*).

SAXS Structure Refinement. Refinement against the scattering data was carried out using CNS as previously described (*46*). The data were sparsened for such calculations by a factor of 18, resulting in a total of 58 data points between

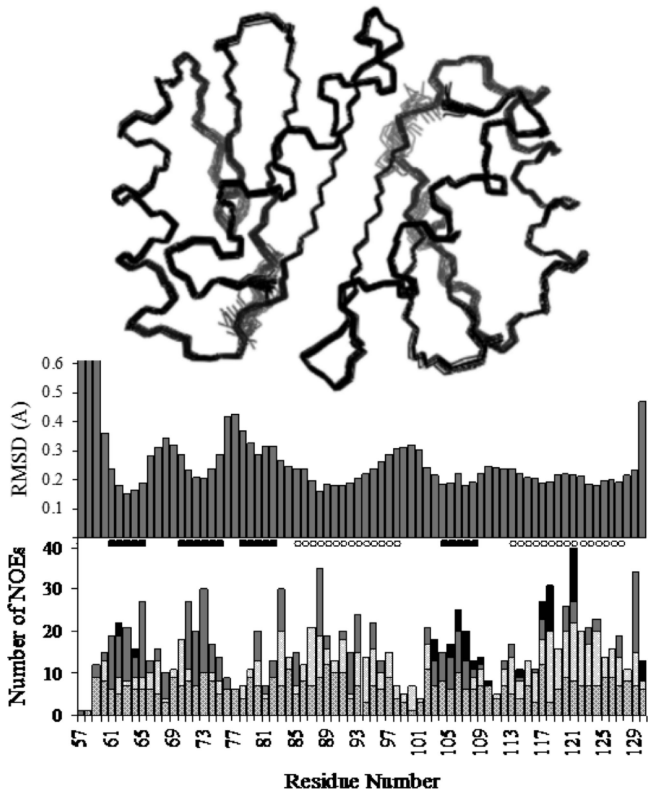

FIGURE 3: NMR-derived backbone for TolR59–130, including uncertainties. Top: Backbone (N, C^{α}, C') overlay of 20 structures. Middle: Backbone rmsd per residue. Bottom: Number of interresidue NOEs per residue. Medium gray bars = sequential restraints, light gray bars = medium range, dark gray bars = long range, and black bars = intersubunit restraints. The secondary structure is shown between the two charts. Solid squares are residues in β strands. Empty circles are residues in helices.

0.02 and 0.60 $Å^{-1}$. Structure refinement with SAXS data was performed using the scattering data either up to q_{max} = 0.35 $Å^{-1}$ or up to q_{max} = 0.50 $Å^{-1}$. The resulting structures were then validated by predicting the scattering data above these q_{max} values and comparing these with the experimental data not fitted beyond this point. Force constants for fitting the SAXS data were optimized on the basis of the quality of the resulting structures measured by bond, angle, and improper violations, Ramachandran statistics, and MolProbity clash scores and by avoiding changes in rms violations greater than 0.002 Å and 0.03 Hz in the experimental NMR parameters, including NOEs and RDCs.

Light Scattering. The molecular mass of TolR with and without the C-terminal tail was determined by laser light scattering and interferometric refractometry. TolR was subjected to gel filtration chromatography (Superdex 75, 10 × 300 mm) prior to analysis with a DAWN EOS multiangle light scattering detector and an OPTILAB DSP refractometer (Wyatt). Molecular mass was calculated using Astra software (Wyatt). Protein (200 μg) in 50 mM sodium phosphate, 50 mM sodium chloride, and 0.5 mM EDTA, pH 6.7, was injected into a preequilibrated column running at a flow rate of 0.5 mL/min at room temperature.

RESULTS

Chemical Shift Assignments and Mutants. Initially, the NMR study focused on the full periplasmic domain of TolR (residues 39–139). However, about 30% of the backbone and side-chain atoms in this construct could not be assigned due to weak signal and indeterminate connectivity. Residues for which the backbone N and H^N atoms could not be assigned include V42, V65, I68, L83, T89, Q90, V106-N122, H125, L126, and K130−I139 (Figure 4F). However, most of the residues for the first three strands and the first helix could be assigned in the TolR39–139 construct and, when later compared to the TolR59–130 clone, were found to form the same structure based on NOE data collected on both samples, as well as close similarity in C^{α} chemical shifts. The assignments that could be made for TolR39–139 are given in Table 1 of Supporting Information. From these limited assignments it was possible to determine the protein's fold using NOEs, TALOS-predicted backbone torsion angles, and hydrogen bonds obtained from secondary structure as indicated by chemical shifts or predicted secondary structure. The tertiary structure helped to pinpoint problematic regions in the protein that were subsequently altered in order to form a more "NMR-friendly" construct. On the basis of the partial structure and on published literature which indicated that the C-terminal tail may interact with the membrane (*25*), the C-terminal nine residues beyond I129, the last assignable residue, were removed. This resulted in clone TolR39–130, which yielded greatly improved spectral appearance over TolR39–139 (Figure 5). To further improve the spectral appearance, a third clone lacking residues 39−58 was constructed. These residues, which connect the transmembrane helix to the structured domain, were highly flexible based on a lack of $^1H-^1H$ NOE connectivities and low ^{15}N R_2 relaxation rates (data not shown). The chemical shifts of residues in the TolR59–130 clone did not differ significantly from their counterparts in TolR39–139, confirming that residues 39−58 do not affect the structure of the periplasmic domain (Figure 5). For the TolR59–130 clone, 100% of the backbone and 96% of the side chains were assigned. The dimer interface was identified by making a mixed protein sample where the majority of the dimer complexes were composed of one unlabeled and one $^{13}C/^{15}N$-labeled monomer (see Experimental Procedures). A filtered ^{13}C-separated NOESY-HSQC experiment identified a substantial number of NOEs between protons in the labeled monomer and protons in the unlabeled monomer (Table 1).

NMR-Only Structure. The secondary structure of each monomer has a β-β-β-α-β-α order with the first three strands lying in a consecutive antiparallel order and the fourth strand lying parallel to the first. The two α-helices are on the same side of the sheet. The first helix stretches diagonally across the first three strands while the second helix runs parallel to β4. The helices form an angle of about 27° to one another when viewed from above the sheet. When looking parallel to the surface of the sheet, the helices form a 45° angle due to a twist in the sheet. As a result, residues A127 and I129 at the C-terminus of α2 have NOE contacts to the center of α1.

The periplasmic domain of TolR forms a dimer based on gel filtration and light scattering experiments. In the dimer, the β4 strands formed by residues 105−109 pair in an antiparallel manner, resulting in an eight-stranded β-sheet. The subunits are oriented so that all four helices are on one side of the β-sheet with the α2 helices from each monomer lying antiparallel to one another. In the dimer, the two

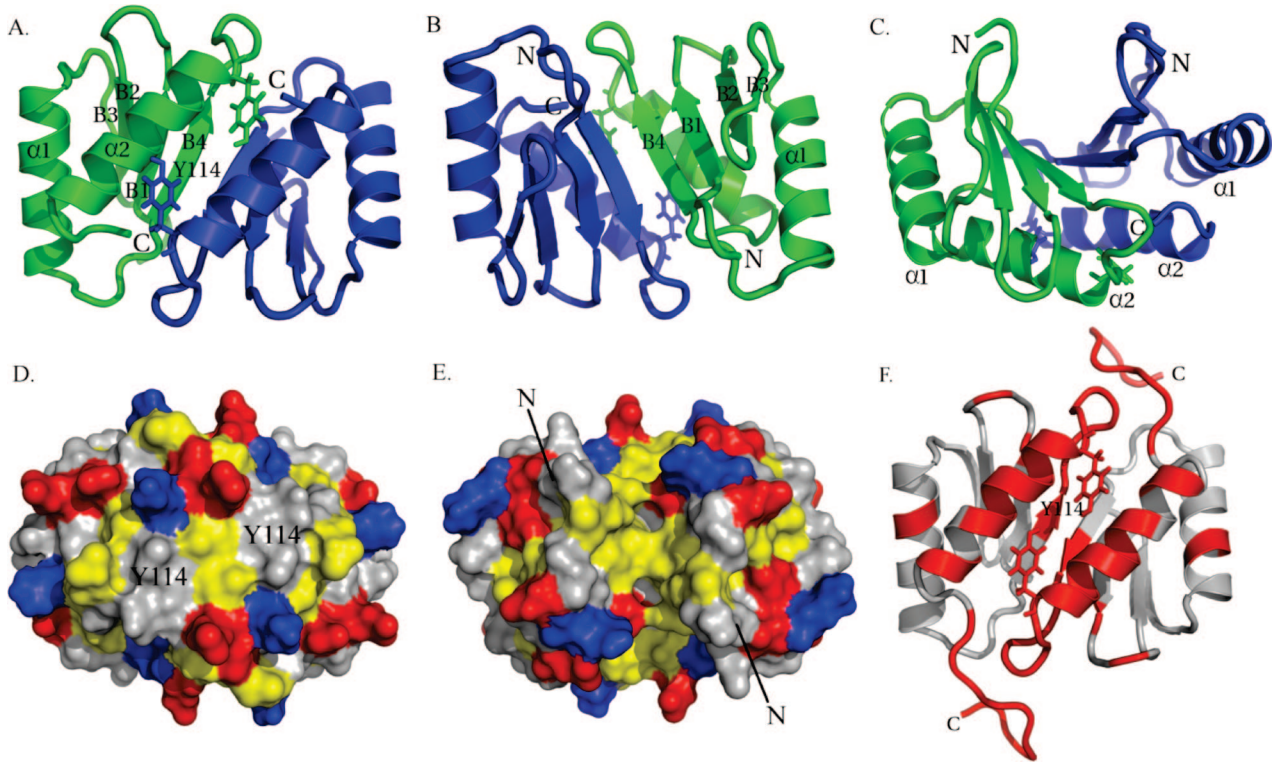

FIGURE 4: Ribbon diagrams and surface models of TolR. (A−C) TolR59–130 with monomers in green and blue. Secondary structure units are labeled. (B) is rotated 180° around the vertical axis of (A). (C) is rotated 90° around the horizontal axis of (A). (D, E) Surface models of TolR59–130. Ala, Leu, Val, Ile, Phe, and Pro are colored yellow. Lys and Arg are in blue. Asp and Glu are in red. (D) and (E) are oriented the same as (A) and (B), respectively. (F) TolR59–130 with residues 131–139 modeled in. ^{15}N and $^{1}H^{N}$ assignments for the TolR39–139 clone could not be made for the residues shown in red.

monomeric sheets are twisted and angled by about 74° relative to each other such that they form a deep groove (about 10 Å deep, 10 Å wide, and 22 Å long) in the middle of the dimeric sheet. As a result, the protein has a flattened U-shape with the α1 helices on the sides and the α2 helices at the bottom (Figure 4).

Backbone ^{15}N relaxation data for TolR59–130 are shown in Figure 6. As this clone lacks the floppy N-terminal residues and the problematic C-terminal tail, the R_1, R_2, and $^{15}N-\{^{1}H\}$ NOE relaxation rates are fairly uniform throughout the protein with only small differences in the loop regions. Exceptions include the first few N-terminal residues, which remain from the longer N-terminal tail, and G67, which is located in the turn between β1 and β2.

Impact of SAXS Refinement. The scattering data recorded at 4 and 8 mg/mL protein concentrations exhibit indistinguishable Guinier regions (lowest scattering angles), aside from the decreased scattered photon counts at the lower protein concentration. This indicates an absence of interparticle interference effects, compatible with the modest protein concentration and relatively high salt concentration within the sample. The data at the lowest scattering angles exhibit linear Guinier plots (Figure 7, insert), supporting the absence of aggregation. The data collected at 8 mg/mL were used for all subsequent structural analyses. Globbic and bound surface water corrections were calculated iteratively after each round of refinement and required two cycles to converge. The final surface solvent layer contrast was determined to be 0.02 e/Å^3, close to the "typical" value of 0.03 e/Å^3 reported for other proteins (*47*). From the structural quality statistics, the structures obtained by fitting scattering data up to $q_{max} = 0.35$ Å^{-1}, which corresponds to a maximum resolution of 18 Å, proved superior with respect to those calculated by fitting SAXS data up to 0.50 Å^{-1} (~12 Å resolution), while perfectly reproducing the entire experimental scattering curve up to $q_{max} = 0.60$ Å^{-1} (Figure 7). For that reason, the final structure refinement was performed by fitting SAXS data up to $q_{max} = 0.35$ Å^{-1} only. These data, which effectively encode the low-resolution shape of the protein, can be fitted quite accurately because globbic corrections remain negligible (≤1%) within this q range. The starting "NMR-only" structures already produce a good fit to the experimental SAXS data (green line, Figure 7). The final structures obtained by a joint SAXS/NMR data fit are quite close to the NMR-only models (backbone rmsd between the two dimers equals ~0.7 Å for residues 60–129), in line with a fairly modest improvement (~7%) of the quality of the fit (χ) of the structural model to the SAXS data as a result of refinement against it (blue line, Figure 7). The orientations of all secondary structure elements remain very similar to those in NMR-only structures. When the β-sheets of the two structures are superimposed (with a backbone rmsd of ca. 0.5 Å), a slight translation of the peripheral α-helices is observed in the NMR-SAXS structures with respect to the NMR-only structures (see Figure 1 in Supporting Information). The α2 helix moves slightly away (ca. 0.5 Å) from the β-sheet and the α1 helix moves ca. 0.7 Å closer to the β-sheet.

Dimer Assembly from RDC and SAXS Data. An interesting question is whether SAXS data and RDCs would be sufficient to determine the relative arrangement of the two chains within the dimer, without any information from interdomain NOE restraints, which often can be more difficult to identify. To investigate this issue, the two monomer units

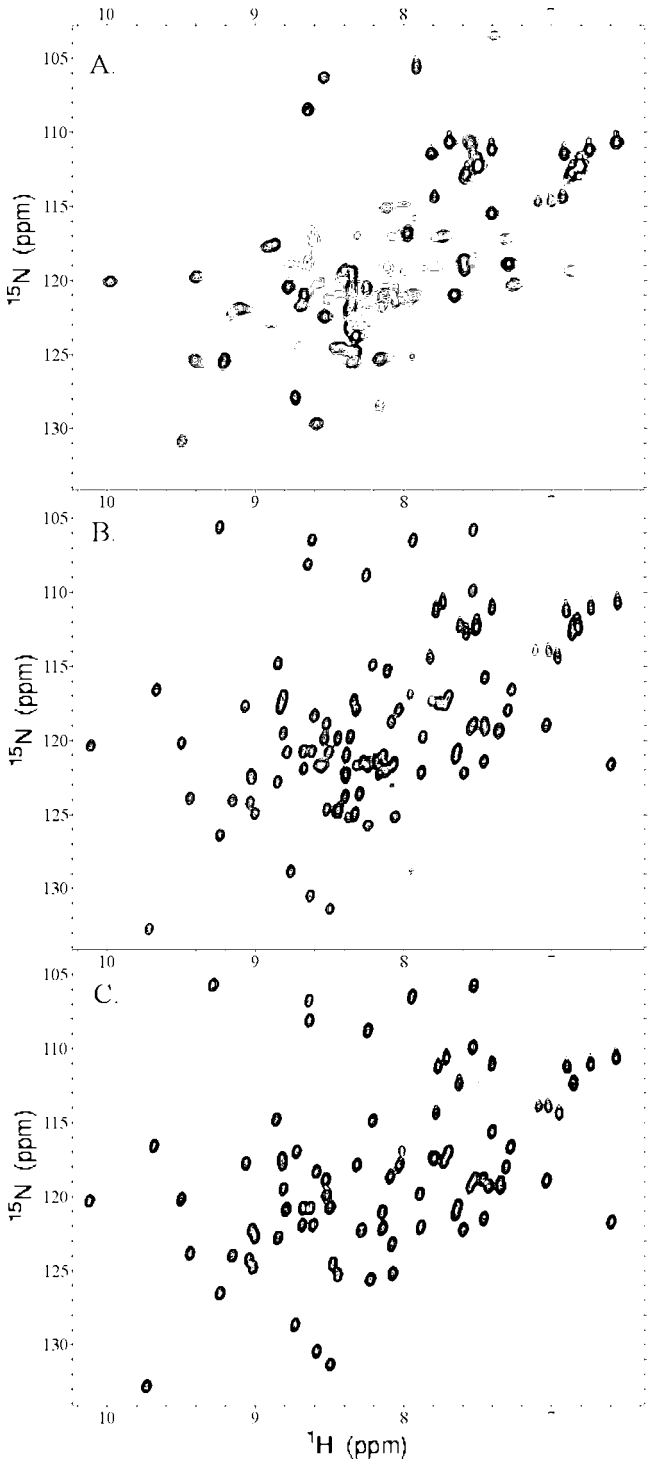

FIGURE 5: ^{1}H−^{15}N-HSQC spectra, recorded at 600 MHz, for (A) TolR39–139, (B) TolR39–130, and (C) TolR59–130.

of the TolR dimer (denoted here by A and B) were separated, and the orientation of the molecular alignment tensor was determined by the SVD (singular value decomposition) fit to the N−H^{N} RDCs. Considering that the dimer yields only a single set of resonances in the 2D HSQC spectrum, it must be C_2 symmetric, with the symmetry axis parallel to one of the three principal axes of the alignment tensor, allowing for a total of four relative orientations that cannot be distinguished on the basis of RDCs measured in a single alignment medium (*48*). These four orientations for B correspond to the orientation of A, and that of A rotated by 180° around each of the three axes of the alignment tensor,

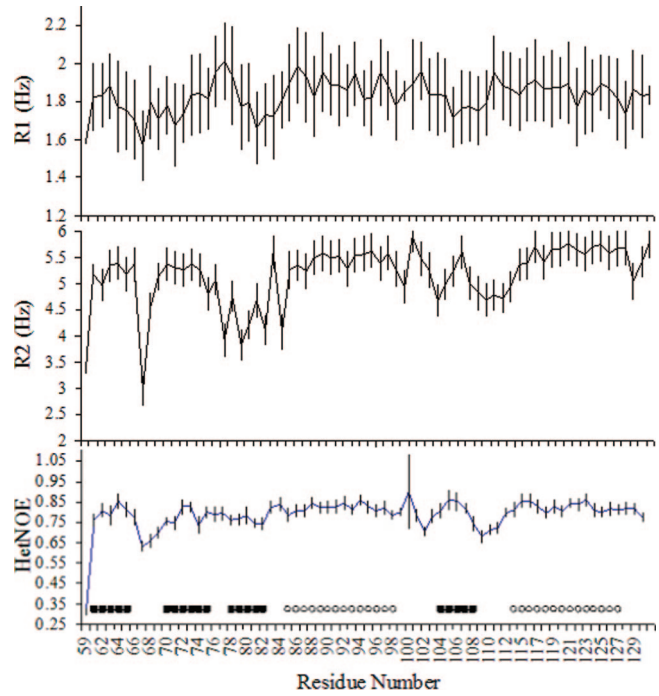

FIGURE 6: Relaxation data for TolR59–130. R_1 = ^{15}N longitudinal rates, R_2 = ^{15}N transverse rates, and HetNOE = ^{15}N−{^{1}H} heteronuclear NOE. The estimated standard errors for R_1 and R_2 and propagated uncertainties for HetNOE values are depicted as vertical lines. Bottom: Secondary structure of TolR59–130: black squares, residues in strands; empty circles, residues in helices.

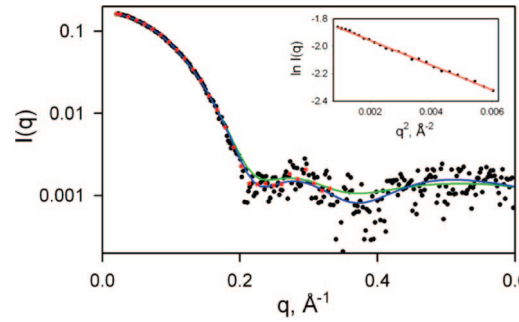

FIGURE 7: Superimposition of the desmeared experimental X-ray scattering data for TolR (black dots) and the sparsened subset of data that are fitted in the NMR-SAXS structure calculation (red dots) with the scattering profiles fitted from the NMR-only (green line) and NMR/SAXS-refined homodimeric structures (blue line). The inset shows the Guinier plot for the lowest angle data.

denoted here by D_x, D_y, and D_z (Figure 8A). The case where B has the same orientation as A cannot result in a C_2 symmetric dimer and therefore can be excluded, and only the remaining three need to be considered. Unit B was then translated in each of these three orientations around unit A on a 50 Å radius sphere, using a Fibonacci number-based vector grid. The maximum order of the grid was set to 21, resulting in 17712 vectors that uniformly covered the sphere and were separated by angular steps of ca. 1.5°. Requirement of the C_2 dimer symmetry then strongly limits the possible arrangements of the two units. These allowed arrangements are selected by evaluating the rmsd between two sets of atoms: [A(60–94) and B(95–128)] versus [B(60–94) and A(95–128)] following the idea previously described in ref *49*. For C_2 symmetry, very low rmsd values will be obtained for these atom selections. To allow for sufficient sampling in the proximity of the correct C_2 axis, we selected all

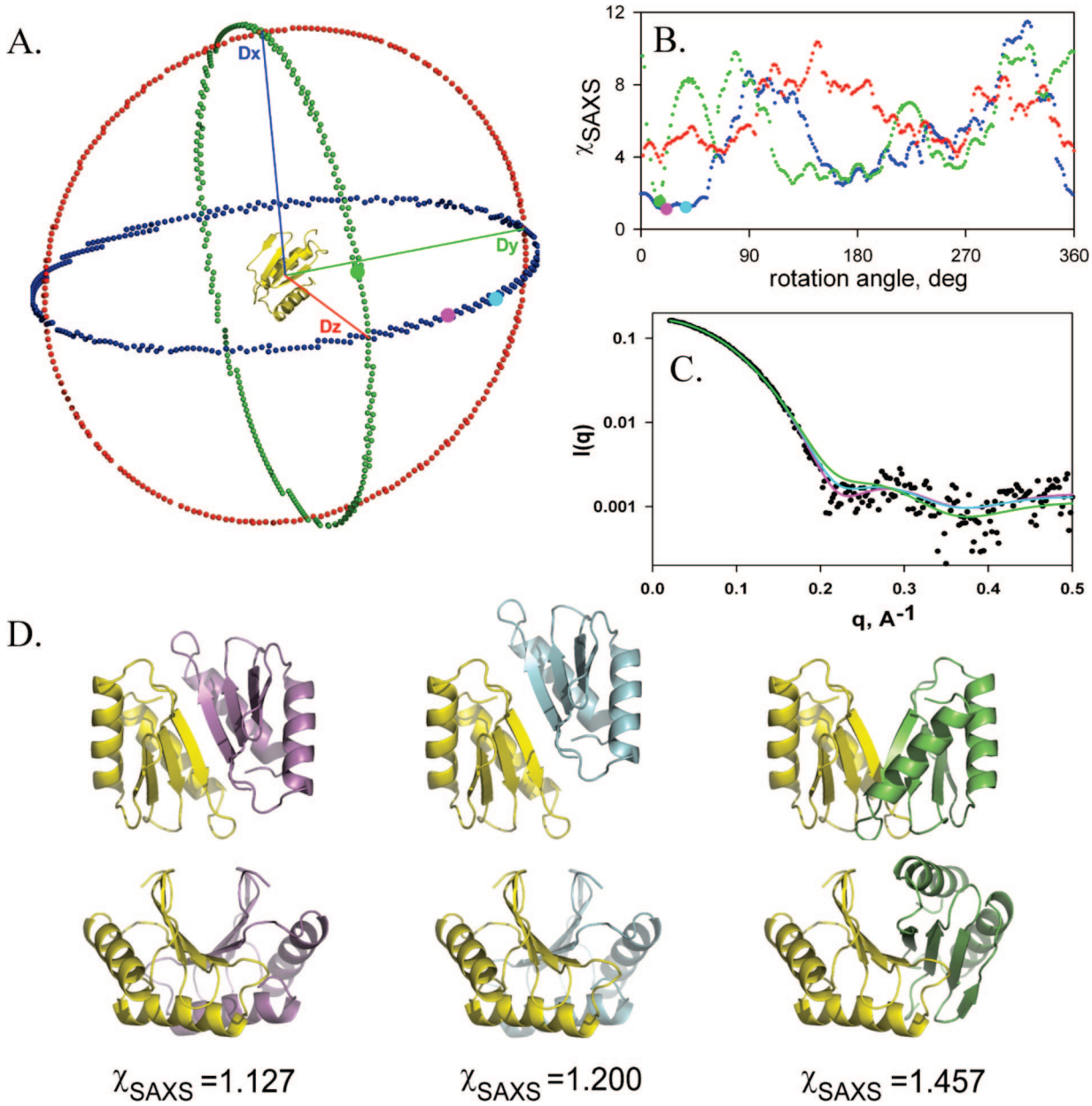

FIGURE 8: Finding the dimer interface using SAXS and RDC data. (A) Schematic representation of the relative arrangements of the TolR domains tested during the dimer assembly. Domain A (shown in yellow) is fixed at the origin of the RDC alignment tensor frame, defined by principal axes D_x, D_y, and D_z. C_2 symmetry requires that the orientation of domain B must correspond to the orientation of domain A, rotated by 180° about either D_x, D_y, or D_z. The coordinates for the centers of mass of domain B that are compatible with the C_2 dimer symmetry are shown as solid dots, all selected from the quasi-uniform 17712 vector grid. Blue dots correspond to the case were D_x is the C_2 axis (correct solution), green and red dots correspond to the cases where the C_2 axis would have been along the D_y and D_z axes, respectively. The angular coordinates that produce the three geometries best fitting to the SAXS data are indicated with magenta, cyan, and green circles (in the order of increasing χ_{SAXS}). (B) Quality of the SAXS data fit for each sphere in (A). The directions for the right-handed rotation angles are as follows: for the correct orientation (blue points), the angle shown is to the D_z axis and the rotation is around D_x; for the orientation corresponding to 180° rotations around D_z (green points), the angle shown is to D_z and the rotation is around $-D_x$; for the orientation corresponding to 180° rotations around D_y (red points), the angle shown is to D_x and the rotation is around D_z. The positions of the three best fitting geometries are shown in magenta, cyan, and green in the order of increasing χ_{SAXS} and correspond to those indicated in (A). (C) Fits of the three dimer geometries to the desmeared experimental scattering data (black dots) with the color scheme matching (A). (D) The three best fitting, closest approach geometries shown in two orthogonal views with the color scheme matching (A). The structure with the lowest χ_{SAXS} exhibits 0.8 Å backbone rmsd to the correct model.

translated geometries that exhibited backbone rmsd values below 0.25 Å for further analysis. After imposing the C_2 restraint, the spherical distribution of translated B units is reduced to thin rings orthogonal to each of the three possible C_2 dimer axis orientations (Figure 8A). Using the 0.25 Å rmsd threshold then results in 250–280 possible translations of the B domain around A for each of the three orientations, or about 800 A−B pairs. For each of these pairs, the B domain subsequently was moved stepwise along the translation vector toward the A domain until a 2.8 Å interdomain contact was observed between atom sets that included C′, C^{α}, N, O, and C^{β}. The resulting geometries were then tested against the experimental scattering data using Crysol 2.6 software (*45*). The results of the fits, shown in Figure 8, indicate that a correct dimer assembly, with a backbone rmsd of 0.8 Å to the target structure and $\chi_{SAXS} = 1.127$ (magenta

circle in Figure 8), could be identified, based entirely on the goodness of fit to the SAXS data. The best fitting model reproduces the correct interdomain pairing of the two β-strands, even though a slight translational shift remains between the two domains. These results differ from an earlier study (*46*), where we were unable to assemble correctly the two domains of γS crystallin based on the SAXS data alone. Possible reasons for the present success include the more asymmetrical shape of the TolR domains as opposed to the pseudo-C_4 symmetry of the γS crystallin domains, usage of the C_2 symmetry restraint in the present case, and a wider angular range and better signal-to-noise statistics of the present SAXS data. The next best fitting solution (cyan circle in Figure 8) corresponds to the correct relative orientation of the two dimer domains and exhibits a 6% higher χ_{SAXS} value. It differs from the correct solution by a two-residue shift in the register of the two β-strands forming the dimer interface. The small difference between the two lowest χ_{SAXS} values, in practice, makes the distinction between the two geometries tenuous, however. The third minimum in χ_{SAXS} corresponds to an incorrect relative orientation of the two domains (green circle in Figure 8) and yields a χ value 30% higher than that of the minimum of the correct solution. The overall shape is strikingly similar to the correct dimer, however, complete with a "groove" formation composed of the β-sheet of one unit and the α2 helix of the other chain. In practice, additional information can be used to verify the best fitting arrangement of the dimer domains, such as the hydrophobic/hydrophilic nature of the buried/exposed surfaces, as well as $^1H/^2H$ exchange protection factors of the backbone amides. At a minimum, SAXS data allow selection of a very small number of possible dimer geometries that can subsequently be evaluated with additional data.

DISCUSSION

Conservation and Structural Homologues. A BLAST (*50*) search for sequences similar to TolR retrieves matches in over 100 Gram-negative bacterial species. Most of the strictly conserved residues are located in or immediately after the transmembrane helix, the exception being Y114, which is conserved in both the TolR and ExbD proteins (Figure 2). Not including Y114, the few residues conserved in the periplasmic domain appear to have structural roles as their side chains all point to the interior of the protein. The two Y114 residues (one from each monomer) lie between the α2 helices at the dimer interface with one edge of each ring exposed on the surface (Figure 4). Two residues, I118 from each monomer, pack between them. It was reported that a Y117C mutant in *E. coli* (Y114 in *H. influenzae*) forms a disulfide bond that affects the function of TolR (*26*). In the *H. influenzae* structure, the $C^\beta-C^\beta$ distance between the two tyrosine residues is 15 Å, which is too large to accommodate the formation of a disulfide bond. Thus, the observed effects of the mutant could result from an improperly formed dimer interface.

Recently, the solution structure of ExbD from *E. coli* was described (*51*). While the secondary and tertiary structures of the two proteins are similar with a Dali-calculated rmsd of 2.4 Å (*52*), the ExbD structure is that of a monomer rather than a dimer. This may be due to the experimental conditions required to obtain the structure. Like TolR, the ExbD protein

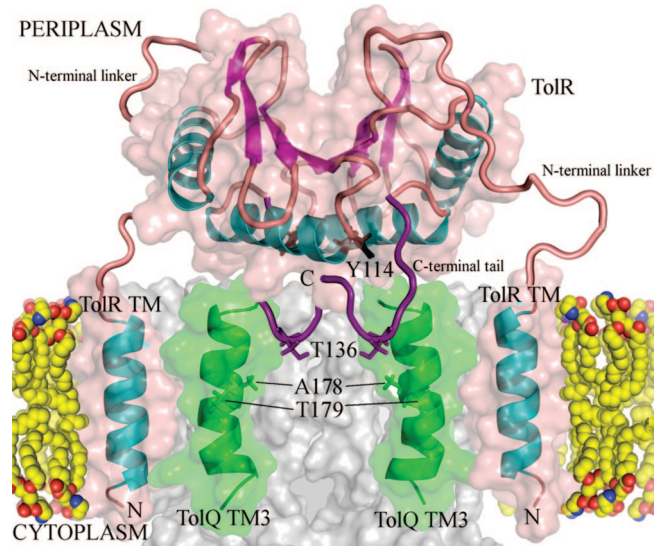

FIGURE 9: Hypothetical model of the TolR interaction with the membrane and TolQ. Structure of TolR59–130 shown as blue/magenta/pink ribbon diagram with pink surface model superimposed. The transmembrane domain of TolR (TolR TM), residues 39–58, and residues 131–139 (in purple) have been modeled. A representative TolQ structure is shown in gray with the third transmembrane helix in green (TolQ TM3). Membrane lipids are shown as yellow, blue, and red balls. A178 and T179 from TolQ (A177 and T178 in *E. coli*) are shown as sticks as are Y114 (shown in black) and T136 in TolR (Y117 and T139 in *E. coli*).

was not readily amenable to NMR. In the case of ExbD, this was because of line broadening caused by protein aggregation. The authors were able to complete the structure by lowering the pH to 3.0 and the protein concentration to 0.2 mM. In the ExbD structure the first few N-terminal residues of the slightly longer C-terminal tail form a short β-strand along β4 which is at the dimer interface in the TolR structure. The remaining residues in the C-terminal tail are present but unstructured. Interestingly, increasing the pH or the concentration of ExbD resulted in the disappearance of peaks in the C-terminal half of β4 and the N-terminal half of α2. The corresponding residues in TolR were also missing or could not be assigned when the C-terminal tail was present.

Searches of other known protein structures using Dali, SSM (*53*), and MATRAS (*54*) found several proteins with domains or parts of domains matching the fold of TolR, but none except ExbD formed a dimer or contained the conserved tyrosine. A PSI-Blast (*50*) search using four iterations did not retrieve any structures with a sequence homologous to TolR. A Blast search of the PDB retrieved ExbD with 31% sequence identity.

Charge Distribution. Except for the groove formed by the β-sheet, both positive and negatively charged residues are fairly evenly distributed across the surface of TolR (Figures 4D,E). The groove is hydrophobic and presents a likely binding site for another protein or small molecule. It is tempting to speculate that perhaps the second or third domain of TolA binds to TolR in response to the PMF, much like the proposed interaction of TonB to the ExbB/ExbD proteins. As of yet, there are no data to support this hypothesis, however, and the residues are not conserved. The curved β-sheet could also be involved in the interaction of TolR with colicins. Studies are underway to explore this possibility.

Function of the C-Terminal Tail. For many years, researchers have been working under the assumption that the second helix of TolR, which is amphiphilic in nature, inserts into the membrane. For this reason, mutational studies have been based on a three-domain model of TolR. The first domain (TolRI) was thought to consist of the transmembrane helix, the second (TolRII), consisting of residues 38−111 (residues 41 to 114 in *E. coli*), and the third domain (TolRIII), which was thought to include the second helix and the C-terminal tail. On the basis of the NMR structure presented here this model is incorrect. The hydrophobic residues along the second helix fit nicely into the hydrophobic core of the protein. In addition, there is no evidence that the helix flips between the protein and the membrane as deuterium exchange rates for amide protons in the interior of the protein (strands β1, β2, and β4 and the α2 helix) are much slower than those in the loops and the exterior β3 strand (Figure 2) as would be expected for an integral part of a protein. Even in the full-length periplasmic clone, side-chain assignments for the methyl groups of interior hydrophobic residues of the second helix could be made, implying that the molecular motions affecting backbone assignments for those residues do not reach all the way into the core of the protein.

Part of the reason the second helix was assumed to insert into the membrane was because studies of the *E. coli* TolR periplasmic portion with the proposed third domain could be found partially associated with the membrane, whereas the second domain (TolRII) which lacked α2 was not (*25*). In *E. coli*, an A177V mutant in the middle of the third transmembrane domain of TolQ is rescued by changing the threonine in the C-terminal tail of TolR to a methionine (T136 in *H. influenzae*). While this does not prove that the two residues are close together, it does suggest the possibility. Perhaps the C-terminal tail alone is responsible for the previously noted membrane association and either inserts directly into the membrane or interacts with membrane-bound TolQ.

The question remains as to why the presence of the tail is so detrimental to structure determination. It could be simply that because the residues in the tail are not anchored to the membrane as they would be *in vivo*, they may interact transiently with the periplasmic domain, broadening the line widths of the atoms involved so that they could not be assigned by NMR. A more interesting possibility, however, is that the interaction is functionally relevant. Not only is the full periplasmic construct completely soluble up to at least 1.0 mM, some fraction of it is found free of the membrane in the above-mentioned study (*25*). It therefore is conceivable that the tail fluctuates between the membrane and the dimer interface *in vivo*.

Relationship of the TolR Periplasmic Domain to the Inner Membrane. A final and perhaps more important question is how the periplasmic domain of TolR is oriented relative to the membrane. As a dimer, it is anchored to the membrane by its two N-terminal transmembrane domains with long, 15−20-residue unstructured stretches of amino acids which do not interact with the main periplasmic domain as evidenced by a lack of chemical shift differences between the TolR39–130 and TolR59–130 constructs. It is probably important to note here that although the TolR39–139 clone did not indicate any structure for residues V40, V42, L44, and P45, they are conserved hydrophobic residues and therefore are likely to interact with another part of the complex. Assuming the shorter C-terminal tail also inserts into the membrane, TolR would have a total of four tethers. This leaves two possible orientations for TolR: either the β-sheet side or the α-helical side faces the membrane. It is more likely that the helices face the membrane for several reasons. First, the N-terminal β-strand would be more distant from the membrane, which could explain why there are so many unstructured residues between the transmembrane helix and the structured portion of the periplasmic part protein. Second, mutating Y117 in *E. coli* (Y114 in *H. influenzae*), which would be close to the membrane if the helices were oriented toward the membrane, rescues a T178 mutant in the third TolQ transmembrane domain (*14*). As mentioned previously, Y114 is highly conserved, and this suggests it may be involved in the function of TolR. Third, *E. coli* cysteine mutants at the ends of the second helix but not in the center are susceptible to modification by MPB [*N*α-(3-maleimidylpropionyl)biocytin] when TolR is membrane bound, suggesting that the center of the helix is closely associated with the membrane or another protein (*26*). The mutants most strongly labeled correspond to residues P113, E115, L126, and K130. Upon disruption of the proton motive force (PMF) several cysteine residues in the center of the helix, namely, those replacing Y114, E116, I118, K119, L121, N122, and H125, become more strongly labeled although not to the extent of the first four residues (*26*). These residues are solvent accessible in the NMR structure and/or at the dimerization interface of the helices. Protection prior to PMF disruption would be consistent with a close interaction between the helices and the inner membrane TolQ/TolR complex. Interestingly, cysteine mutants of all but the last three residues of the C-terminal tail were also protected from MPB modification with S134C, G136C, and T139C (S131, G133, and T136 in *H. influenzae*) becoming somewhat exposed when the PMF was disrupted. If the tail does interact with TolQ or the membrane, then TolR must face the membrane with its helices because the length of the C-terminal tether on each side of the protein would be limited to two residues, much too short to wrap around TolR if the helices were facing the periplasm. Figure 9 demonstrates a hypothetical TolQ/TolR/membrane arrangement.

CONCLUSIONS

The structure of TolR, presented here, shows an α-β fold that is shared by several proteins, including its homologue ExbD, but the TolR structure differs from all of them in that it forms a dimer. Modeling the protein with the helices facing the membrane and the C-terminal tail inserted into the membrane, the structure explains how the second helix and C-terminal tail can be in the vicinity of mutants in the third TolQ transmembrane domain. In addition, the hydrophobic groove in the β-sheet is intriguing because it suggests something, perhaps TolA, may bind in this location.

Methodologically, we demonstrated the utility of RDCs and SAXS data in lieu of intersubunit NOE restraints for the construction of a nondomain-swapped dimer. In conclusion, the completed structure of the TolR periplasmic domain demonstrates that TolR has two domains and a C-terminal tail rather than the proposed three domains. It verifies the

presence of a dimer, reveals an intriguing hydrophobic groove, and, along with mutational data, provides information regarding the orientation of the periplasmic portion of TolR relative to the inner membrane.

ACKNOWLEDGMENT

We thank Dr. John Louis for conducting the light scattering measurements and Dr. John Orban for stimulating discussion.

SUPPORTING INFORMATION AVAILABLE

Table 1, providing chemical shift assignments for TolR39–139, and Figure 1, providing a superposition of the NMR-only and NMR-SAXS structures. This material is available free of charge via the Internet at http://pubs.acs.org.

REFERENCES

1. Sturgis, J. N. (2001) Organisation and Evolution of the tol-pal Gene Cluster. *J. Mol. Microbiol. Biotechnol. 3*, 113–122.
2. Guihard, G., Boulanger, P., Benedetti, H., Lloubes, R., Besnard, M., and Letellier, L. (1994) Colicin A and the Tol proteins involved in its translocation are preferentially located in the contact sites between the inner and outer membranes of *Escherichia coli* cells. *J. Biol. Chem. 269*, 5874–5880.
3. Walburger, A., Lazdunski, C., and Corda, Y. (2002) The Tol/Pal system function requires an interaction between the C-terminal domain of TolA and the N-terminal domain of TolB. *Mol. Microbiol. 44*, 695–708.
4. Dubuisson, J. F., Vianney, A., and Lazzaroni, J. C. (2002) Mutational Analysis of the TolA C-terminal domain of *Escherichia coli* and Genetic Evidence for an Interaction between TolA and TolB. *J. Bacteriol. 184*, 4620–4625.
5. Cascales, E., Gavioli, M., Sturgis, J. N., and Lloubes, R. (2000) Proton motive force drives the interaction of the inner membrane TolA and outer membrane pal proteins in Escherichia coli. *Mol. Microbiol. 38*, 904–915.
6. Bernadac, A., Gavioli, M., Lazzaroni, J. C., Raina, S., and Lloubes, R. (1998) *Escherichia coli* tol-pal mutants form outer membrane vesicles. *J. Bacteriol. 180*, 4872–4878.
7. Cascales, E., Bernadac, A., Gavioli, M., Lazzaroni, J. C., and Lloubes, R. (2002) Pal lipoprotein of *Escherichia coli* plays a major role in outer membrane integrity. *J. Bacteriol. 184*, 754–759.
8. Llamas, M. A., Ramos, J. L., and Rodriguez-Herva, J. J. (2000) Mutations in Each of the tol Genes of *Pseudomonas putida* Reveal that they are Critical for Maintenance of Outer Membrane Stability. *J. Bacteriol. 182*, 4764–4772.
9. Gerding, M. A., Ogata, Y., Pecora, N. D., Niki, H., and de Boer, P. A. (2007) The trans-envelope Tol-Pal complex is part of the cell division machinery and required for proper outer-membrane invagination during cell constriction in *E. coli*. *Mol. Microbiol. 63*, 1008–1025.
10. Braun, V., and Herrmann, C. (1993) Evolutionary relationship of uptake systems for biopolymers in *Escherichia coli*: cross-complementation between the TonB-ExbB-ExbD and the TolA-TolQ-TolR proteins. *Mol. Microbiol. 8*, 261–268.
11. Davies, J. K., and Reeves, P. (1975) Genetics of resistance to colicins in *Escherichia coli* K-12: cross-resistance among colicins of group B. *J. Bacteriol. 123*, 96–101.
12. Letain, T. E., and Postle, K. (1997) TonB protein appears to transduce energy by shuttling between the cytoplasmic membrane and the outer membrane of *Escherichia coli*. *Mol. Microbiol. 24*, 271–283.
13. Cascales, E., Lloubes, R., and Sturgis, J. N. (2001) The TolQ-TolR proteins energize TolA and share homologies with the flagellar motor proteins MotA-MotB. *Mol. Microbiol. 42*, 795–807.
14. Goemaere, E. L., Cascales, E., and Lloubes, R. (2007) Mutational analyses define helix organization and key residues of a bacterial membrane energy-transducing complex. *J. Mol. Biol. 366*, 1424–1436.
15. Llamas, M. A., Rodriguez-Herva, J. J., Hancock, R. E., Bitter, W., Tommassen, J., and Ramos, J. L. (2003) Role of *Pseudomonas putida* tol-oprL gene products in uptake of solutes through the cytoplasmic membrane. *J. Bacteriol. 185*, 4707–4716.
16. Murphy, T. F., Bartos, L. C., Rice, P. A., Nelson, M. B., Dudas, K. C., and Apicella, M. A. (1986) Identification of a 16,600-dalton outer membrane protein on nontypeable *Haemophilus influenzae* as a target for human serum bactericidal antibody. *J. Clin. Invest. 78*, 1020–1027.
17. Lubkowski, J., Hennecke, F., Pluckthun, A., and Wlodawer, A. (1999) Filamentous phage infection: crystal structure of g3p in complex with its coreceptor, the C-terminal domain of TolA. *Structure 15*, 711–722.
18. Click, E. M., and Webster, R. E. (1998) The TolQRA proteins are required for Membrane Insertion of the Major Capsid Protein of the Filamentous Phage f1 during Infection. *J. Bacteriol. 180*, 1723–1728.
19. Rabsch, W., Ma, L., Wiley, G., Najar, F., Kaserer, W., Schuerch, D., Klebba, J., Roe, B., Laverde-Gomez, J., Schallmey, M., Newton, S., and Klebba, P. (2007) FepA- and TonB-dependent bacteriophage H8: receptor binding and genomic sequence. *J. Bacteriol. 189*, 5658–5674.
20. Hausler, T. (2006) *Viruses vs. Superbugs: A Solution to the Antibiotics Crisis?*, Macmillan, New York.
21. Parsons, L. M., Lin, F., and Orban, J. (2006) Peptidoglycan Recognition by Pal, an Outer Membrane Lipoprotein. *Biochemistry 45*, 2122–2128.
22. Bonsor, D., Grishkovskaya, I., Dodson, E., and Kleanthous, C. (2007) Molecular mimicry enables competitive recruitment by a natively disordered protein. *J. Am. Chem. Soc. 129*, 4800–4807.
23. Witty, M., Sanz, C., Shah, A., Grossman, J., Mizuguchi, K., Perham, R., and Luisi, B. (2002) Sructure of the periplasmic domain of *Pseudomonas aeruginosa* TolA: evidence for an evolutionary relationship with the TolB transproter protein. *EMBO J. 21*, 4207–4218.
24. Kampfenkel, K., and Braun, V. (1993) Membrane Topologies of the TolQ and TolR proteins of *Escherichia coli*: Inactivation of TolQ by a Missense Mutation in the Proposed First Transmembrane Segment. *J. Bacteriol. 175*, 4485–4491.
25. Journet, L., Rigal, A., Lazdunski, C., and Benedetti, H. (1999) Role of TolR N-terminal, central, and C-terminal domains in dimerization and interaction with TolA and tolQ. *J. Bacteriol. 181*, 4476–4484.
26. Goemaere, E. L., Devert, A., Lloubes, R., and Cascales, E. (2007) Movements of the TolR C-terminal domain depend on TolQR ionizable key residues and regulate activity of the Tol complex. *J. Biol. Chem. 282*, 17749–17757.
27. Hansen, M., Mueller, L., and Pardi, A. (1998) Tunable alignment of macromolecules by filamentous phage yields dipolar coupling interactions. *Nat. Struct. Biol. 5*, 1065–1074.
28. Cavanagh, J., Fairbrother, W. J., Palmer, A. G., III, Skelton, N. J., and Rance, M. (2007) *Protein NMR Spectroscopy: Principles and Practice*, Elsevier Academic Press, Burlington, VT.
29. Chou, J. J., Delaglio, F., and Bax, A. (2000) Measurement of one-bond ^{15}N-$^{13}C'$ couplings in medium sized proteins. *J. Biomol. NMR 18*, 101–105.
30. Kontaxis, G., Clore, G. M., and Bax, A. (2000) Evaluation of cross correlation effects and measurement of one-bond couplings in proteins with short transverse relaxation times. *J. Magn. Reson. 143*, 184–196.
31. Hu, J.-S., Grzesiek, S., and Bax, A. (1997) Two-dimensional NMR methods for determining $\chi 1$ angles for aromatic residues in proteins from three-bond $J_{C'-C\gamma}$ and $J_{N-C\gamma}$ couplings. *J. Am. Chem. Soc. 119*, 1803–1809.
32. Farrow, N. A., Muhandiram, R., Singer, A. U., Pascal, S. M., Kay, C. M., Gish, G., Shoelson, S. E., Pawson, T., Forman-Kay, J. D., and Kay, L. E. (1994) Backbone dynamics of a free and phosphopeptide-complexed Src homology 2 domain studied by ^{15}N NMR relaxation. *Biochemistry 33*, 5984–6003.
33. Bax, A. (2003) Weak alignment offers new NMR opportunities to study protein structure and dynamics. *Protein Sci. 12*, 1–16.
34. Zweckstetter, M., and Bax, A. (2002) Evaluation of uncertainty in alignment tensors obtained from dipolar couplings. *J. Biomol. NMR 23*, 127–137.
35. Clore, G. M., and Garrett, D. S. (1999) R-factor, Free R, and Complete Cross-Validation for Dipolar Coupling Refinement of NMR structures. *J. Am. Chem. Soc. 121*, 9008–9012.
36. Delaglio, F., Grzesiek, S., Vuister, G. W., Zhu, G., Pfeifer, J., and Bax, A. (1995) NMRPipe: a multidimensional spectral processing system based on UNIX pipes. *J. Biomol. NMR 6*, 277–293.

37. Goddard, T. D., and Kneller, D. G. SPARKY 3, University of California, San Francisco.
38. Parsons, L. M. (2003) *Structural Genomics of Hypothetical Proteins from Haemophilus influenzae by NMR Spectroscopy*, University of Maryland, College Park, MD.
39. DeLano, W. L. (2002) DeLano Scientific, San Carlos, CA.
40. Brunger, A. T., Adams, P. D., Clore, G. M., DeLano, W. L., Gros, P., Grosse-Kunstleve, R. W., Jiang, J. S., Kuszewski, J., Nilges, M., Pannu, N. S., Read, R. J., Rice, L. M., Simonson, T., and Warren, G. L. (1998) Crystallography & NMR system: A new software suite for macromolecular structure determination. *Acta Crystallogr., Sect. D: Biol. Crystallogr. 54* (5), 905–921.
41. Grishaev, A., and Bax, A. (2004) An Empirical Backbone-Backbone Hydrogen-Bonding Potential in Proteins and Its Applications to NMR Structure Refinement and Validation. *J. Am. Chem. Soc. 126*, 7281–7292.
42. Laskowski, R. A., Rullmannn, J. A., MacArthur, M. W., Kaptein, R., and Thornton, J. M. (1996) AQUA and PROCHECK-NMR: programs for checking the quality of protein structures solved by NMR. *J. Biomol. NMR 8*, 477–486.
43. Davis, I. W., Leaver-Fay, A., Chen, V. B., Block, J. N., Kapral, G. J., Wang, X., Murray, L. W., Arendall, W. B., III, Snoeyink, J., Richardson, J. S., and Richardson, D. C. (2007) MolProbity: all-atom contacts and structure validation for proteins and nucleic acids. *Nucleic Acids Res. 35*, 375–383.
44. Svergun, D. I. (1992) Determination of the regularization parameter in indirect-transform methods using perceptual criteria. *J. Appl. Crystallogr. 25*, 495–503.
45. Svergun, D. I., Barberato, C., and Koch, M. H. J. (1995) CRYSOL—a Program to Evaluate X-ray Solution Scattering of Biological Molecules from Atomic Coordinates. *J. Appl. Crystallogr. 28*, 768–773.
46. Grishaev, A., Wu, J., Trewhella, J., and Bax, A. (2005) Refinement of multidomain protein structures by combination of solution small-angle X-ray scattering and NMR data. *J. Am. Chem. Soc. 127*, 16621–16628.
47. Svergun, D. I., Richard, S., Koch, M. H. J., Sayers, Z., Kuprin, S., and Zaccai, G. (1998) Protein Hydration in Solution: Experimental observation by x-ray and neutron scattering. *Proc. Natl. Acad. Sci.U.S.A. 95*, 2267–2272.
48. Al-Hashimi, H. M., Valafar, H., Terrell, M., Zartler, E. R., Eidsness, M. K., and Prestegard, J. H. (2000) Variation of molecular alignment as a means of resolving orientational ambiguities in protein structures from dipolar couplings. *J. Magn. Reson. 143*, 402–406.
49. Dam, J., Baber, J., Grishaev, A., Malchiodi, P., Schuck, P., Bax, A., and Mariuzza, J. (2006) Variable Dimerization of the Ly49A Natural Killer Cell Receptor Results in Differential Engagement of its MHC Class I Ligand. *J. Mol. Biol. 362*, 102–113.
50. Altschul, S. F., Madden, T. L., Schaffer, A. A., Zhang, J., Zhang, Z., Miller, W., and Lipman, D. J. (1997) Gapped BLAST and PSI-BLAST: a new generation of protein database search programs. *Nucleic Acids Res. 25*, 3389–3402.
51. Garcia-Herrero, A., Peacock, R. S., Howard, S. P., and Vogel, H. J. (2007) The solution structure of the periplasmic domain of the TonB system ExbD protein reveals an unexpected structural homology with siderophore-binding proteins. *Mol. Microbiol. 66*, 872–889.
52. Holm, L., and Sander, C. (1995) Dali: a network tool for protein structure comparison. *Trends Biochem. Sci. 20*, 478–480.
53. Krissinel, E., and Henrick, K. (2004) Secondary-structure matching (SSM), a new tool for fast protein structure alignment in three dimensions. *Acta Crystallogr. D 60*, 2256–2268.
54. Kawabata, T. (2003) MATRAS: a program for protein 3D structure comparision. *Nucleic Acids Res. 31*, 3367–3369.

BI702283X